metals

MDPI

Communication

Recoverable Deformation Behavior of Ultrathin 30 μm Ti–24Nb–4Zr–8Sn Foils

Jiaxing Wang [1], Siyu Wei [2], Delun Gong [2,*], Xingbin Li [2], Dongmei Chen [1], Rui Zhang [1], Yadong Su [1], Rui Yang [2] and Yulin Hao [2,*]

[1] AVIC Shenyang Aircraft Design & Research Institute, Shenyang 110035, China
[2] Shenyang National Laboratory for Materials Science, Institute of Metal Research, Chinese Academy of Sciences, Shenyang 110016, China
* Correspondence: dlgong17s@imr.ac.cn (D.G.); ylhao@imr.ac.cn (Y.H.)

Abstract

Ultrathin titanium alloy foils are attractive for engineering components requiring flexural compliance and mechanical support, yet their recoverable deformation behavior at the foil scale remains insufficiently characterized. This study evaluates 30 μm Ti–24Nb–4Zr–8Sn (wt.%, Ti2448) foils in the as-rolled and solution-treated states and compares their tensile loading–unloading response with same-thickness CP Ti and Ti–6Al–4V reference foils. The Ti2448 foils exhibit a larger recoverable-deformation window and a lower apparent loading modulus than the reference foils under the same testing protocol. The highest recoverable strain is obtained in the solution-treated longitudinal condition, indicating that the recoverable deformation is sensitive to both processing state and loading direction. These results suggest Ti2448 foils as potential candidates for flexure-related applications requiring large recoverable deformation.

Keywords: Ti–24Nb–4Zr–8Sn alloy; ultrathin titanium foil; metastable β titanium alloy; recoverable deformation response; apparent loading modulus; cyclic loading–unloading

1. Introduction

Ultrathin titanium alloy foils are of interest for lightweight, corrosion-resistant, and compliant metallic components operating at thicknesses of only a few tens of micrometres [1–6]. In foil-scale service modes involving bending, tensile deflection, repeated displacement, or microforming-related deformation, conventional metrics such as strength and formability alone do not fully describe functional performance [1–5]. The strain recovered during unloading and the residual strain accumulated after deformation directly affect dimensional stability, repeatability, and mechanical reliability in thin or flexible titanium-based components [1–5]. Quantifying recoverable strain and residual strain is therefore essential for assessing titanium foils intended for elastic, compliant, or flexure-dominated applications.

Metastable β titanium alloys provide a metallurgical route for improving strain recovery in titanium-based materials [6–14]. Compared with commercially pure Ti (CP Ti) and conventional α+β titanium alloys, metastable β alloys generally exhibit lower loading stiffness and, when β-phase stability and microstructure are appropriately controlled, can show nonlinear elastic, recoverable, or superelastic-like deformation responses [6–14]. Ti–24Nb–4Zr–8Sn, commonly referred to as Ti2448, is a representative Ni-free metastable

Academic Editor: Yanxin Qiao

Received: 17 June 2026
Revised: 30 June 2026
Accepted: 3 July 2026
Published: 4 July 2026

 https://doi.org/10.3390/met16070736

β titanium alloy within the broader Ti-Nb-Sn/Ti-Nb-Zr-Sn family; low stiffness, nonlinear elastic response, martensitic transformation behavior, and recoverable deformation have been investigated in Ti2448 and closely related metastable β-Ti alloys across bulk, bar, plate, and sheet geometries [15–29]. Previous work has shown that the recoverable response of Ti2448 and related metastable β-Ti systems is sensitive to β-phase stability, oxygen content, thermal history, deformation history, crystallographic texture, and microstructural state [20,23–33]. More recent studies have further highlighted the importance of sample size, functional fatigue, dislocation-dependent behavior, thermal–mechanical cycling, texture-controlled anisotropy, room-temperature recovery, athermal ω, and rolling reduction ratio in Ti2448 and related processing routes [34–41]. Despite this substantial body of work, the recoverable deformation behavior of Ti2448 in ultrathin foil form remains insufficiently established.

The response of a 30 μm rolled Ti2448 foil should not be inferred solely by extrapolation from larger Ti2448 geometries. In bulk, bar, plate, and sheet specimens of Ti2448 and closely related metastable β-Ti alloys, low stiffness, nonlinear elasticity, and transformation-related recovery are usually interpreted in terms of alloy chemistry, β-phase stability, texture, and thermomechanical history [15–29,31–41]. At the foil scale, additional factors become important. Rolling to a thickness of 30 μm may retain or redistribute β texture, introduce deformation substructure and local orientation gradients, and generate loading-direction-dependent mechanical behavior [28,34,38,41]. The high surface-to-volume ratio, altered through-thickness constraint, and grain-size/thickness relationship may further change the balance among ordinary elastic recovery, nonlinear β-matrix deformation, possible transformation-related strain, and irreversible slip [1–5,34–37]. These considerations make direct foil-scale evaluation necessary, particularly when the intended loading modes involve bending, tensile deflection, or repeated displacement [1–5,35–37].

In this study, 30 μm Ti2448 foils are evaluated using a same-thickness, direction-resolved testing strategy. As-rolled and solution-treated Ti2448 foils were tested along the longitudinal and transverse directions and compared with same-thickness CP Ti and Ti–6Al–4V reference foils under the same cyclic tensile loading–unloading protocol. Digital image correlation (DIC) was used to measure macroscopic strain during mechanical testing, while electron backscatter diffraction (EBSD) and ex situ high-energy synchrotron X-ray diffraction (SXRD) were used to characterize crystallographic texture, processing-induced structural state, and phase-related signatures. This combined approach allows the recoverable deformation response to be assessed in relation to processing state, retained β texture, apparent loading stiffness, and possible contributions from β-phase instability. The objective is to determine whether a metastable β-based recoverable response is retained after rolling Ti2448 to a thickness of 30 μm, and how this response is affected by post-rolling solution treatment and loading direction.

2. Materials and Methods

Ti–24Nb–4Zr–8Sn (Ti2448) foils were fabricated from 2.0 mm-thick starting stock by multi-pass cold rolling at room temperature along a single rolling direction to a final thickness of 30 μm without intermediate annealing. The total thickness reduction was 98.5%, corresponding to a true thickness strain of approximately 4.20. Commercially pure Ti and Ti–6Al–4V foils with the same nominal thickness of 30 μm were used as reference materials and tested under the same loading–unloading protocol along their rolling directions.

Two Ti2448 processing conditions were examined: the as-rolled 30 μm foil and the post-rolling solution-treated 30 μm foil. The foil was vacuum-sealed in a quartz tube and solution-treated at 750 °C for 1 h; the sealed tube was then air-cooled to room temperature. A β-transus temperature of approximately 677 °C has been reported for Ti2448, and 750 °C has been used as a β-region solution-treatment condition in previous Ti2448 heat-treatment studies [20,31,32]. In the present work, this treatment was used to obtain a comparative post-rolling solution-treated state, not as an optimized condition for maximizing recoverable strain. The rolling direction, transverse direction, and normal direction are denoted as RD, TD, and ND, respectively. Specimens loaded parallel to RD are referred to as longitudinal (L) specimens, whereas those loaded parallel to TD are referred to as transverse (T) specimens.

Uniaxial tensile tests and cyclic tensile loading–unloading tests were conducted using an Instron E10000 universal testing system (Instron, Norwood, MA, USA) universal testing system under displacement control at a nominal engineering strain rate of 2.5×10^{-4} s^{-1}. The cyclic tests were performed as successive loading–unloading steps. Three valid specimens were tested for each reported mechanical condition (N = 3). During mechanical testing, force, crosshead displacement, and DIC-derived gauge-section strain were recorded. Engineering stress was calculated as $\sigma = F/A_0$, where F is the recorded force and A_0 is the initial cross-sectional area. Engineering stress–strain curves were used to determine tensile strength, apparent loading modulus, recoverable strain, and residual strain. Residual strain, ε_{res}, was defined as the strain remaining after unloading to zero nominal stress. Recoverable strain, ε_{rec}, was calculated as $\varepsilon_{rec} = \varepsilon_{max} - \varepsilon_{res}$, where ε_{max} is the applied strain at the beginning of unloading.

Because metastable β-Ti alloys can exhibit nonlinear loading–unloading responses, the stiffness parameter reported here is denoted as the apparent loading modulus, E_{app}, rather than Young's modulus [20,29,31,33–37]. E_{app} was obtained from the initial loading branch of each engineering stress–strain curve by least-squares linear regression over a fixed engineering-strain interval of 0.1–0.5%. The same fitting interval and procedure were applied to all specimens and material conditions. The unloading branch was not used for E_{app} determination because it may be affected by hysteresis, residual strain, nonlinear β-lattice recovery, and possible transformation-related reverse strain. Thus, E_{app} is used as an apparent loading stiffness defined within the present testing protocol.

A two-dimensional digital image correlation (DIC) system was used as a non-contact strain-measurement method during tensile testing. A stochastic speckle pattern was applied to the specimen surface before testing. The DIC data were used to obtain gauge-section-averaged macroscopic strain for stress–strain conversion and strain-recovery analysis. Full-field strain localization and strain heterogeneity were not quantified.

Microstructure and crystallographic texture were characterized by EBSD. EBSD was used to determine grain morphology and crystallographic orientation distributions, and pole figures were reconstructed from the orientation data to evaluate texture differences between the as-rolled and solution-treated states. Because the as-rolled map contains extensive non-indexed regions associated with rolling-induced distortion, it is used mainly to indicate indexing degradation and orientation localization. The EBSD comparison is therefore qualitative and is not used as an equal-footing grain-size comparison between the two states.

High-energy SXRD experiments were carried out at PETRA III, DESY, Hamburg, Germany. A monochromatic X-ray beam with an energy of 83 keV was used, corresponding to a wavelength of 0.1494 Å. Diffraction patterns were collected in transmission geometry using an area detector. The sample-to-detector distance was calibrated using a LaB_6 standard reference material, and the detector geometry and instrumental parameters were determined before measurement. Measurements were conducted on both as-rolled and solution-treated Ti2448 foils. Because SXRD was not performed in situ during tensile loading, the data are used to characterize the processing-induced structural state, β-phase stability, and retained texture.

3. Results

3.1. Phase Structure and Texture of Ti2448 Foils

Figures 1 and 2 summarize the effect of cold rolling and subsequent solution treatment on the structural state of the 30 μm Ti2448 foil. In the as-rolled state, the two-dimensional diffraction pattern consists of broad and diffuse rings rather than sharp Debye–Scherrer rings (Figure 1a). The corresponding integrated profile shows broadened β reflections together with weak α″-related features (Figure 1c). Because peak broadening may arise from both microstrain and refinement of coherently diffracting domains, it is treated here as qualitative evidence of a highly strained deformation structure, not as a single quantified microstructural parameter. The weak α″-related features are consistent with local β-phase instability during severe rolling, although the overall phase constitution remains β-based. Consistently, the EBSD inverse pole figure (IPF) map of the as-rolled foil contains extensive non-indexed regions and elongated orientation domains mainly aligned with the rolling direction (Figure 2a). Together, these observations indicate that cold rolling introduces deformation-induced disorder in the β matrix, including lattice distortion, local orientation gradients, and deformation substructure.

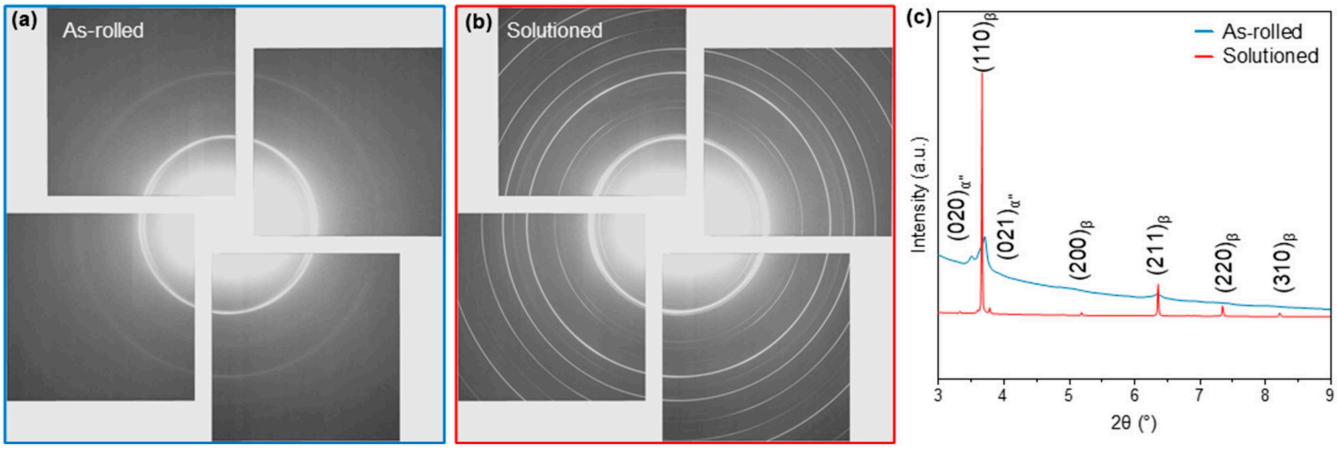

Figure 1. Structural state of 30 μm Ti2448 foils before and after solution treatment. (**a**,**b**) Two-dimensional synchrotron X-ray diffraction patterns of Ti2448 foils in the as-rolled and solution-treated states, respectively. (**c**) Corresponding azimuthally integrated diffraction profiles. The as-rolled foil shows broadened and diffuse β diffraction rings with weak α″-related features. After solution treatment, the diffraction rings become sharper and more continuous, and the integrated profile is dominated by β reflections, indicating partial relaxation of the rolling-induced structural disorder while retaining a β-based phase constitution.

After solution treatment at 750 °C for 1 h, the diffraction rings become sharper and more continuous, and the integrated diffraction profile is dominated by β reflections, including the (110)β peak and higher-order peaks indexed as (200)β, (211)β, (220)β, and (310)β (Figure 1b,c). The weak features tentatively assigned to α″ in the as-rolled foil are treated as qualitative signs of β-phase instability, not as a quantified α″ phase fraction. Because no in situ diffraction was performed during loading, these features do not demonstrate stress-induced transformation during the cyclic tensile tests.

The texture data show that this structural recovery is not accompanied by complete texture randomization. In the as-rolled foil, the non-uniform azimuthal intensity of the diffraction rings indicates preferred orientation, and the β {100}, {101}, and {111} pole figures confirm a pronounced rolling texture (Figures 1a and 2b). The inverse pole figures show clear orientation concentrations along the principal sample directions. The as-rolled foil should therefore be considered a highly deformed and textured β matrix.

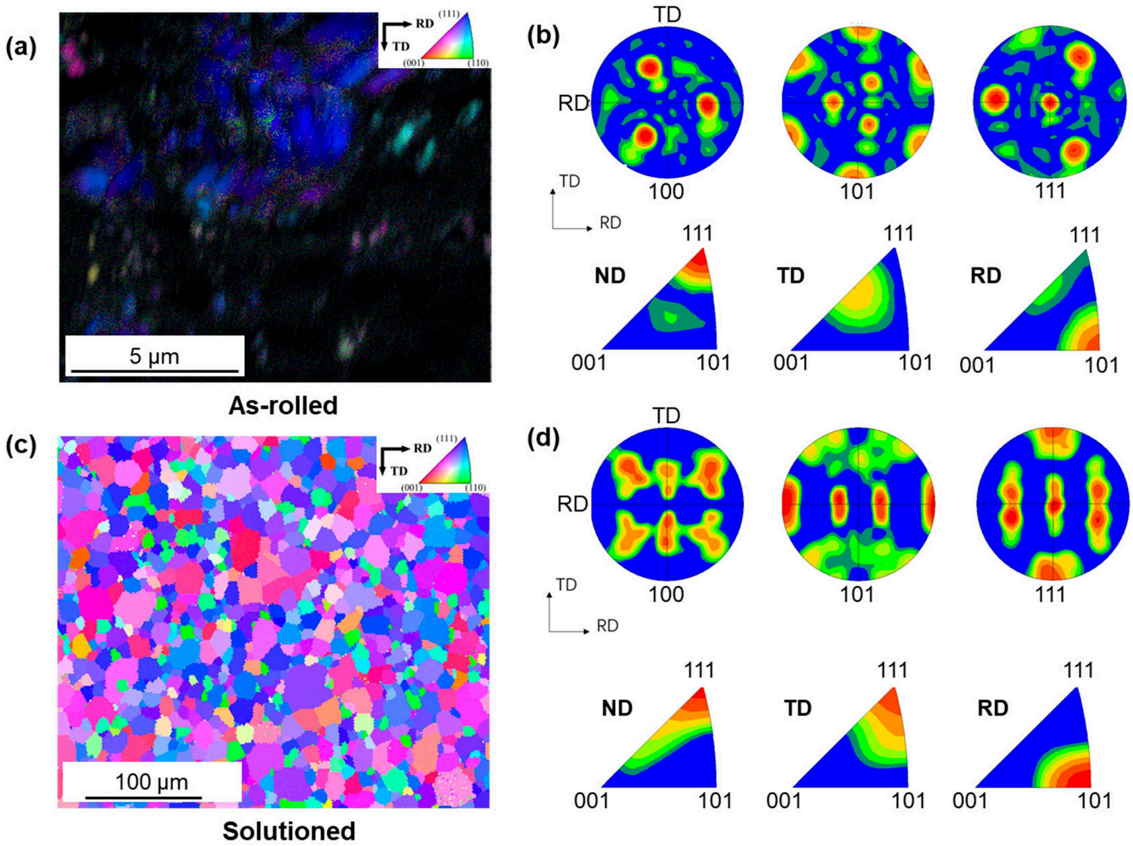

Figure 2. Microstructure and crystallographic texture of 30 µm Ti2448 foils before and after solution treatment. (**a**,**c**) EBSD inverse pole figure orientation maps of the as-rolled and solution-treated foils, respectively. The color coding follows the IPF key shown in each map; RD, TD, and ND denote the rolling, transverse, and normal directions. Non-indexed or poorly indexed regions are displayed in black. (**b**,**d**) Corresponding β-phase {100}, {101}, and {111} pole figures and inverse pole figures along ND, TD, and RD.

After solution treatment, the β texture is redistributed but remains evident. The pole figures are still non-random, and the inverse pole figures along the normal, transverse, and rolling directions retain distinct orientation concentrations (Figure 2d). Although the intensity distribution differs from that of the as-rolled state, the solution-treated foil remains crystallographically anisotropic. Thus, solution treatment reduces the deformation-induced substructure, as reflected by sharper diffraction features and improved EBSD indexing, while preserving a modified β texture.

Taken together, Figures 1 and 2 show that processing history affects the Ti2448 foil through two coupled structural variables: the degree of deformation-induced disorder and the distribution of β-phase crystallographic texture. Cold rolling produces a metastable, defect-rich, and textured β-based structure, whereas solution treatment partially restores structural coherence and changes the texture distribution without eliminating anisotropy.

3.2. Recoverable Deformation Response of Ti2448 Foils

The cyclic tensile responses in Figure 3a–d show recoverable deformation in the 30 µm Ti2448 foils, with clear dependences on loading direction and processing condition. In the as-rolled state, the transverse specimens show a higher mean tensile strength and apparent loading modulus, with UTS = 960 MPa and E_{app} = 61 GPa, whereas the longitudinal specimens show UTS = 915 MPa and E_{app} = 50 GPa (Table 1). The mean recoverable strain is larger along the longitudinal direction (1.9%) than along the transverse direction (1.4%). This comparison establishes a direction-dependent trend in the as-rolled ultrathin foil.

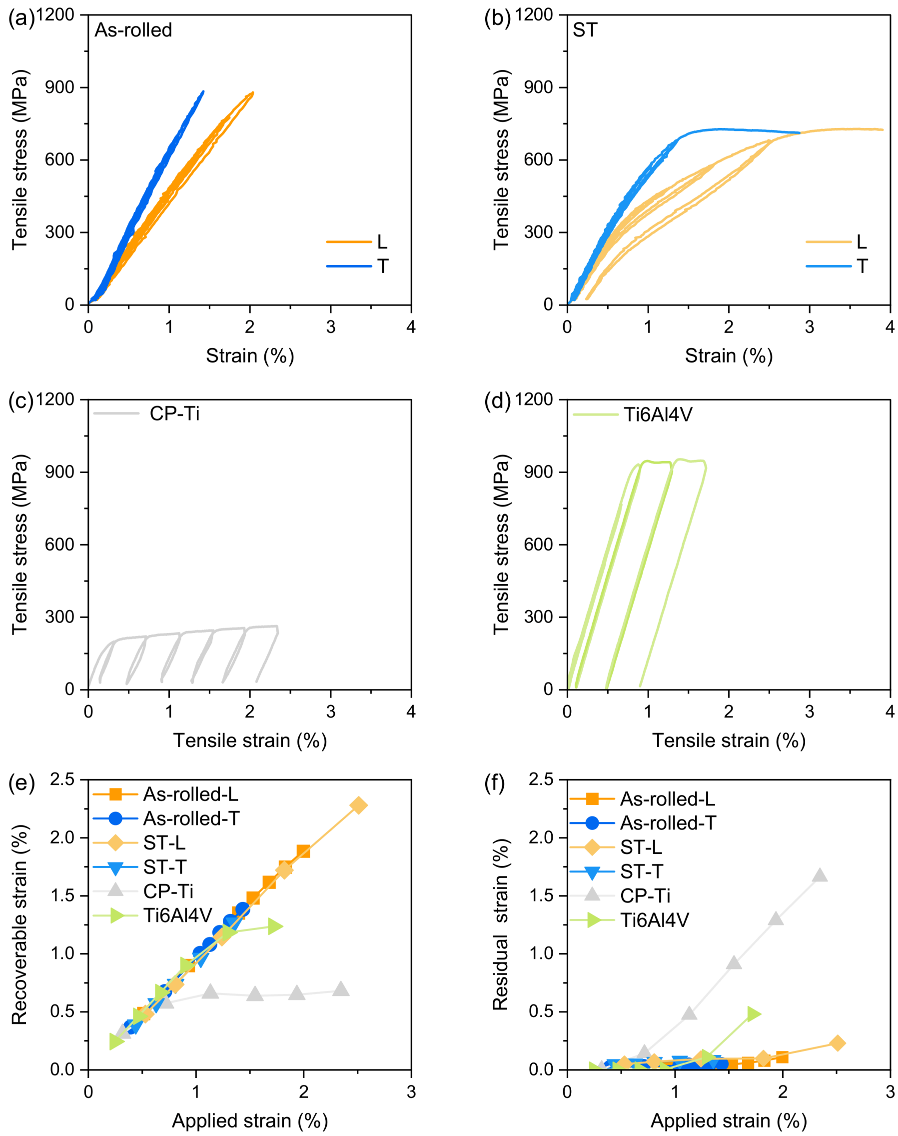

Figure 3. Representative cyclic tensile loading–unloading responses of Ti2448 ultrathin foils and reference CP Ti and Ti–6Al–4V foils. (**a**,**b**) Representative cyclic tensile curves of 0.03 mm Ti2448 foils tested along the longitudinal direction (L, parallel to the rolling direction) and transverse direction (T) in the as-rolled state and after solution treatment at 750 °C for 1 h followed by air cooling, respectively. The stress unit is MPa. In the plotted legends, ST denotes the solution-treated condition. (**c**,**d**) Representative cyclic tensile curves of CP Ti and Ti–6Al–4V reference foils. (**e**,**f**) Recovered strain and residual strain as functions of applied strain.

Table 1. Tensile properties and recoverable strains of Ti2448 and reference foils. Values are reported as means ± SD from three valid specimens per condition (N = 3).

Specimen	UTS [MPa]	E_{app} [GPa]	Recoverable Strain [%]
Ti2448 as-rolled T	960 ± 11	61 ± 4	1.4 ± 0.1
Ti2448 as-rolled L	915 ± 13	50 ± 3	1.9 ± 0.0
Ti2448 solution-treated T	730 ± 9	73 ± 7	1.4 ± 0.1
Ti2448 solution-treated L	724 ± 7	64 ± 5	2.3 ± 0.1
CP Ti	205 ± 5	109 ± 2	0.3 ± 0.0
Ti–6Al–4V	940 ± 8	116 ± 5	0.8 ± 0.0

After solution treatment at 750 °C for 1 h followed by air cooling, the mean tensile strength of Ti2448 decreases to 724–730 MPa, while E_{app} increases to 64–73 GPa (Table 1). The longitudinal specimens reach the largest mean recoverable strain in this study, 2.3%, whereas the transverse specimens reach 1.4%. Thus, solution treatment does not change the recovery response uniformly in all directions: it increases the longitudinal mean value, while the transverse value remains close to that of the as-rolled state within the present comparison. This directional dependence is consistent with the retained β texture shown in Figure 2.

The reference CP Ti (Figure 3c) and Ti–6Al–4V (Figure 3d) foils show different cyclic responses. CP Ti has a low tensile strength of 205 MPa and a recoverable strain of 0.3%, consistent with early accumulation of permanent strain after yielding. Ti–6Al–4V sustains a much higher tensile strength of 940 MPa but reaches a recoverable strain of only 0.8% under the same testing conditions. The recovered- and residual-strain plots in Figure 3e,f highlight this contrast: Ti2448 maintains a larger recovered-strain fraction with limited residual-strain accumulation over the examined range, whereas CP Ti and Ti–6Al–4V show a more conventional elastic-plastic partitioning after yielding.

3.3. Comparison with CP Ti and Ti–6Al–4V Foils

Figure 4 gives a representative longitudinal-direction comparison with the same-thickness CP Ti and Ti–6Al–4V reference foils, whereas Table 1 lists the mean UTS, E_{app}, and recoverable-strain values from three valid specimens per condition. The E_{app} of Ti2448 ranges from 50 to 73 GPa depending on processing condition and loading direction, whereas CP Ti and Ti–6Al–4V show E_{app} values of 109 and 116 GPa, respectively. The lower E_{app} of Ti2448 contributes to a wider recoverable deformation range, but the direction-dependent recovery within Ti2448 also indicates roles for texture and metastable β-based deformation.

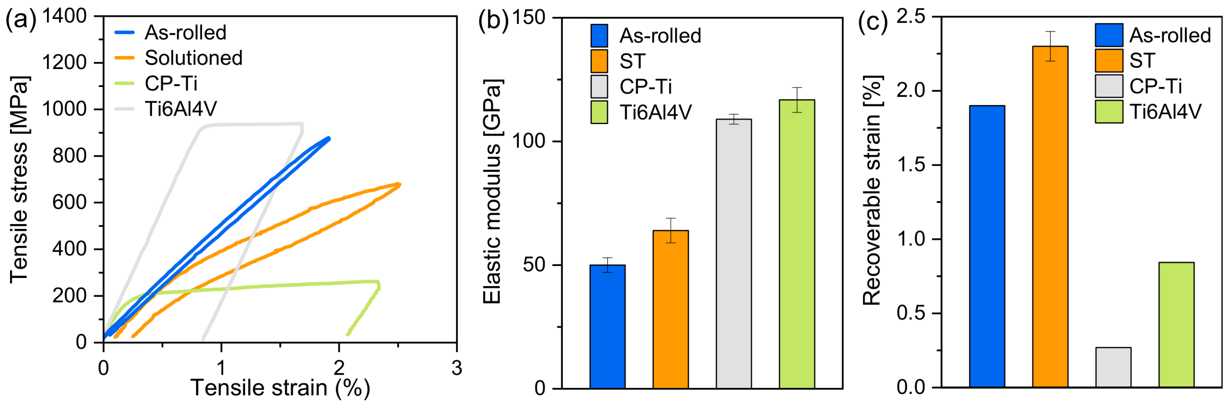

Figure 4. Representative longitudinal-direction comparison of recoverable tensile deformation among Ti2448, CP Ti, and Ti–6Al–4V foils. (**a**) Representative loading–unloading tensile curves of 0.03 mm Ti2448 foils in the as-rolled and solution-treated states along L, together with CP Ti and Ti–6Al–4V reference foils of the same thickness. (**b**,**c**) Apparent loading modulus, E_{app}, and recoverable strain values for the corresponding longitudinal comparison.

The mean recoverable strain of Ti2448 is higher than that of the reference foils under the present testing conditions. The as-rolled Ti2448 foils recover 1.9% in the longitudinal direction and 1.4% in the transverse direction, while the solution-treated foils recover 2.3% and 1.4%, respectively (Table 1). The longitudinal values plotted in Figure 4c provide the direct visual comparison with CP Ti and Ti–6Al–4V, which recover 0.3% and 0.8%, respectively.

Overall, the combined results in Figures 3 and 4 and Table 1 show that ultrathin Ti2448 foils provide a larger mean recoverable-strain window than CP Ti and Ti–6Al–4V foils of the same thickness under the present testing conditions. The highest mean recoverable strain is obtained in the solution-treated longitudinal condition, while the transverse Ti2448 values also exceed those of the reference foils within the present comparison.

https://doi.org/10.3390/met16070736

4. Discussion

4.1. Recoverable Deformation Window of 30 μm Ti2448 Foils

The same-thickness comparison provides the first basis for interpreting the mechanical advantage of the 30 μm Ti2448 foils. Under the present cyclic tensile loading–unloading protocol, the mean recoverable strain of Ti2448 ranges from 1.4% to 2.3%, whereas the same-thickness CP Ti and Ti–6Al–4V reference foils recover approximately 0.3% and 0.8%, respectively. Because the reference foils were tested with the same nominal thickness and under the same protocol, the larger recovery of Ti2448 cannot be attributed to foil thickness alone. Instead, it reflects the distinct deformation response of the metastable β Ti2448 alloy state. The lower recoverability of CP Ti and Ti–6Al–4V is consistent with the more conventional elastic–plastic response expected for thin commercially pure titanium and α+β titanium alloy foils after yielding [1–5], whereas metastable β titanium alloys can accommodate recoverable deformation through lower stiffness, nonlinear β-matrix deformation, and transformation-related mechanisms when β-phase stability is suitably controlled [6–14].

The apparent loading modulus further distinguishes Ti2448 from the reference foils. Depending on processing state and loading direction, Ti2448 shows E_{app} values of 50–73 GPa, compared with 109 GPa for CP Ti and 116 GPa for Ti–6Al–4V. This lower apparent stiffness reduces the stress associated with a given recoverable strain and is consistent with the low-modulus and nonlinear elastic behavior previously reported for Ti2448 and related metastable β-Ti alloys [15–21,24–29]. However, E_{app} alone does not determine the magnitude of recovery within the Ti2448 foils. After solution treatment, the longitudinal specimen exhibits the highest recoverable strain even though its E_{app} is higher than that of the as-rolled longitudinal specimen. This indicates that recovery in the 30 μm foils is controlled not only by apparent stiffness, but also by the processing-modified β structural state, resistance to irreversible slip, and orientation of the retained texture relative to the loading axis.

The measured recovery is therefore best described as macroscopic recoverable deformation. The recoverable strain includes conventional elastic recovery and additional reversible or partially reversible deformation of the metastable β matrix. The residual strain records the part of the deformation accommodated by irreversible slip and by structural rearrangements that are not recovered during unloading. This partitioning is consistent with the nonlinear loading–unloading curves, the low E_{app} values, and the measurable residual strains of Ti2448. Previous studies on Ti2448 and related metastable β-Ti alloys have shown that recoverable deformation can be affected by β/α'' stability, oxygen content, thermal history, stress history, dislocation-dependent behavior, room-temperature recovery, and cyclic evolution [20,24–29,31,33,35–39]. The present data fit within this broader Ti2448 framework, while emphasizing how these effects appear in an ultrathin rolled-foil geometry.

4.2. Role of Processing State and Retained β Texture

Foil rolling and solution treatment modify the recoverable response through two coupled factors: the structural state of the metastable β matrix and the crystallographic texture inherited from rolling. In the as-rolled condition, SXRD shows broadened β diffraction features with weak α''-related signatures, and EBSD shows extensive non-indexed regions, elongated orientation domains, and pronounced rolling texture. These features indicate a cold-worked β-based state containing deformation-induced disorder, local orientation gradients, and retained texture. Similar sensitivity of Ti2448 to thermomechanical history, microstructural state, β-phase stability, athermal ω, and rolling reduction has been reported in larger or differently processed Ti2448 materials [20,23,30–32,40–45]. The higher tensile strength of the as-rolled specimens is consistent with a higher resistance to plastic flow, but a highly strained rolling structure does not necessarily maximize recovery because stored defects and local orientation gradients can also promote residual strain during unloading.

Solution treatment at 750 °C for 1 h changes this balance. The sharper β diffraction features and improved EBSD indexing indicate partial relaxation of the rolling-induced deformation structure, while the decrease in tensile strength shows a reduction in the resistance to plastic flow. At the same time, the β texture remains non-random. This combination is consistent with the direction-selective change in recoverable strain: the longitudinal recoverable strain increases to 2.3%, whereas the transverse value remains close to that of the as-rolled transverse foil. The treatment therefore improves the structural coherence of the β matrix without eliminating the orientation anisotropy introduced by rolling.

The longitudinal/transverse difference is one of the key features of the 30 μm Ti2448 foils. In both processing states, the longitudinal specimens, loaded parallel to RD, show larger mean recoverable strain than the transverse specimens, loaded parallel to TD. Conversely, the transverse direction exhibits a higher E_{app}. This pairing of higher apparent stiffness with lower recovery indicates that the orientation of the retained β texture relative to the tensile axis affects axial compliance and recoverable strain. Such a relationship is consistent with the elastic anisotropy of Ti2448 single crystals and with reported texture effects in Ti2448 and related β-Ti materials [21,28,38,41]. In the present work, the EBSD and SXRD data establish the existence of retained texture and its persistence after solution treatment. A quantitative assignment of the anisotropy to specific slip systems, Schmid factor distributions, Taylor factor differences, or martensitic variant selection would require orientation-resolved deformation measurements, in situ tensile diffraction, or crystal-plasticity-based analysis. The appropriate interpretation here is therefore a texture-linked anisotropic recoverable response.

4.3. Relation to Larger Ti2448 Geometries and Application Implications

The present 30 μm foil results connect with the established understanding of Ti2448 in bulk, bar, plate, and sheet geometries, but they also define a distinct foil-scale problem. Previous work has shown that Ti2448 and closely related metastable β-Ti systems can exhibit low stiffness, nonlinear β response, α′′-related transformation behavior, gum-like or superelastic recovery, and strong sensitivity to thermal history, microstructure, texture, stress history, dislocation state, cyclic loading, sample size, and rolling reduction [15–45]. The present foils show the same general metastable β-Ti character, as indicated by their low E_{app}, nonlinear loading–unloading response, β-dominated structural state, retained texture, and processing-dependent diffraction features. However, rolling to 30 μm introduces a more severe foil-processing route and changes the geometric constraints relative to bulk, bar, plate, and conventional sheet specimens. The increased surface-to-volume ratio, reduced through-thickness constraint, grain-size/thickness relationship, and foil-relevant loading modes such as bending or displacement-controlled deformation may all influence the competition between recoverable β-matrix deformation and irreversible slip [1–5,34].

The structural characterization supports the mechanical interpretation while defining the level of mechanistic resolution. EBSD establishes the retained β texture, processing-dependent indexing quality, and elongated orientation domains associated with rolling. Ex situ high-energy SXRD identifies the β-based structural state, retained diffraction texture, processing-dependent broadening or sharpening of β reflections, and weak α′′-related features in the as-rolled condition. These observations are consistent with a metastable β matrix capable of accommodating recoverable deformation through compliant and nonlinear β-based response. At the same time, the SXRD measurements were not collected during loading–unloading. They therefore provide a structural basis for interpreting the initial and solution-treated states, but they do not track $\beta \rightarrow \alpha''$ formation, reverse transformation, or load-path-dependent phase evolution in the present foils. Prior in situ diffraction and high-energy X-ray studies have directly shown transformation-related processes in Ti2448 and related Ti–Nb alloys [14,26,29], so an α''-related contribution remains physically plausible. In this work, however, it is treated as a possible component of the recoverable response.

The combination of low E_{app} and 1.4–2.3% recoverable strain indicates potential use for small compliant foil components where low apparent stiffness and limited residual deformation are desirable. Examples include micro-springs, micro-diaphragms, MEMS-like compliant structures, flexible electronic support or strain-relief components, and biomedically relevant flexible elements [1–6]. These applications involve loading modes and service histories that are not fully represented by the present tensile loading–unloading protocol. In particular, functional fatigue, thermal–mechanical cycling, and dislocation-dependent evolution are known to influence the recovery behavior of Ti2448 [33,35–37,39]. Further work should therefore focus on extended tensile cycling, bending fatigue, strain-rate and temperature effects, full-field strain mapping, and in situ structural characterization during loading–unloading. Such studies will be needed to separate nonlinear β elasticity, possible α''-related transformation, and irreversible slip more quantitatively, and to assess the practical reliability of Ti2448 foils in flexure-dominated engineering components.

5. Conclusions

Thirty-micrometer Ti2448 foils retain a large recoverable deformation response after severe foil rolling and post-rolling solution treatment. Under the present cyclic tensile loading–unloading protocol, the mean recoverable strain ranged from 1.4% to 2.3%, exceeding those of same-thickness CP Ti and Ti–6Al–4V reference foils. The highest mean recoverable strain was obtained in the solution-treated longitudinal condition. The longitudinal/transverse difference, together with the retained β texture observed by EBSD and SXRD, indicates a texture-linked anisotropic recovery response. The lower apparent loading modulus of Ti2448, together with its β-based structural state, supports further assessment of 30 μm Ti2448 foils for flexure-dominated components. However, the separate contributions of nonlinear β elasticity, possible α''-related transformation, and irreversible slip should be further resolved by in situ diffraction, extended cyclic testing, and bending-fatigue evaluation in the future.

Author Contributions: Conceptualization, D.G., R.Y. and Y.H.; methodology, J.W., S.W., D.G., X.L., D.C., R.Z. and Y.S.; software, J.W., S.W. and D.G.; validation, J.W., S.W., D.G., X.L., D.C., R.Z., Y.S., R.Y. and Y.H.; formal analysis, J.W., S.W., D.G., X.L., D.C., R.Z. and Y.S.; investigation, J.W., S.W., X.L., D.C., R.Z. and Y.S.; resources, D.G., X.L., D.C., R.Z., Y.S., R.Y. and Y.H.; data curation, J.W., S.W., D.G., X.L., D.C., R.Z. and Y.S.; writing—original draft preparation, J.W., S.W. and D.G.; writing—review and editing, J.W., S.W., D.G., X.L., D.C., R.Z., Y.S., R.Y. and Y.H.; visualization, J.W., S.W. and D.G.; supervision, D.G., R.Y. and Y.H.; project administration, D.G., X.L., D.C., R.Z., Y.S., R.Y. and Y.H.; funding acquisition, D.G., X.L., D.C., R.Z., Y.S., R.Y. and Y.H. All authors have read and agreed to the published version of the manuscript.

Funding: This research was funded by the National Key Research and Development Program of China, grant number 2023YFC2412600.

Data Availability Statement: The data presented in this study are available on request from the corresponding author. The data are not publicly available because they are part of an ongoing research project.

Acknowledgments: Synchrotron experiments were performed at beamline P21.2 of PETRA III, DESY, Hamburg, Germany, a member of the Helmholtz Association, under Proposal Nos. I-20250831 and I-20240938. The authors thank Malte Blankenburg, Zoltan Hegedüs, Sven Gutschmidt, and Ulrich Lienert for the experimental support at DESY.

Conflicts of Interest: The authors declare no conflicts of interest. The funder had no role in the design of the study; in the collection, analyses, or interpretation of data; in the writing of the manuscript; or in the decision to publish the results.

Nomenclature

Abbreviation	**Meaning**
DIC	Digital image correlation
EBSD	Electron backscatter diffraction
SXRD	Synchrotron X-ray diffraction
RD	Rolling direction
TD	Transverse direction
ND	Normal direction
L	Longitudinal specimen, with loading axis parallel to RD
T	Transverse specimen, with loading axis parallel to TD
UTS	Ultimate tensile strength
E_{app}	Apparent loading modulus determined from the initial loading branch
N	Number of valid specimens tested for each condition

References

1. Zheng, Q.; Shimizu, T.; Shiratori, T.; Yang, M. Tensile properties and constitutive model of ultrathin pure titanium foils at elevated temperatures in microforming assisted by resistance heating method. *Mater. Des.* **2014**, *63*, 389–397. [CrossRef]
2. Zheng, Q.; Shimizu, T.; Yang, M. Effect of heat on tensile properties of thin pure titanium foils. *Manuf. Rev.* **2015**, *2*, 3. [CrossRef]
3. Guo, B.; Wang, W.; Kong, B.; Wang, Z.; Kong, C.; Yu, H. Development of low anisotropic commercially pure titanium foils by asymmetric rolling and annealing. *Adv. Eng. Mater.* **2024**, *26*, 2400248. [CrossRef]
4. Wang, L.; Zhang, H.; Huang, G.; Cao, M.; Cao, X.; Mostaed, E.; Vedani, M. Formability and anisotropy of the mechanical properties in commercially pure titanium after various routes normal and different speed rolling. *J. Mater. Res.* **2016**, *31*, 3372–3380. [CrossRef]
5. Galán-López, J.; Verleysen, P. Simulation of the plastic response of Ti–6Al–4V thin sheet under different loading conditions using the viscoplastic self-consistent model. *Mater. Sci. Eng. A* **2018**, *712*, 1–11. [CrossRef]
6. Niinomi, M.; Nakai, M.; Hieda, J. Development of new metallic alloys for biomedical applications. *Acta Biomater.* **2012**, *8*, 3888–3903. [CrossRef] [PubMed]
7. Kolli, R.P.; Devaraj, A. A review of metastable beta titanium alloys. *Metals* **2018**, *8*, 506. [CrossRef]
8. Kim, H.Y.; Ikehara, Y.; Kim, J.I.; Hosoda, H.; Miyazaki, S. Martensitic transformation, shape memory effect and superelasticity of Ti–Nb binary alloys. *Acta Mater.* **2006**, *54*, 2419–2429. [CrossRef]
9. Kim, H.Y.; Miyazaki, S. Martensitic transformation and superelastic properties of Ti–Nb base alloys. *Mater. Trans.* **2015**, *56*, 625–634. [CrossRef]
10. Kim, H.Y.; Sasaki, T.; Okutsu, K.; Kim, J.I.; Inamura, T.; Hosoda, H.; Miyazaki, S. Texture and shape memory behavior of Ti–22Nb–6Ta alloy. *Acta Mater.* **2006**, *54*, 423–433. [CrossRef]
11. Al-Zain, Y.; Kim, H.Y.; Hosoda, H.; Nam, T.H.; Miyazaki, S. Shape memory properties of Ti–Nb–Mo biomedical alloys. *Acta Mater.* **2010**, *58*, 4212–4223. [CrossRef]
12. Al-Zain, Y.; Kim, H.Y.; Koyano, T.; Hosoda, H.; Nam, T.H.; Miyazaki, S. Anomalous temperature dependence of the superelastic behavior of Ti–Nb–Mo alloys. *Acta Mater.* **2011**, *59*, 1464–1473. [CrossRef]
13. Ijaz, M.F.; Kim, H.Y.; Hosoda, H.; Miyazaki, S. Effect of Sn addition on stress hysteresis and superelastic properties of a Ti–15Nb–3Mo alloy. *Scr. Mater.* **2014**, *72–73*, 29–32. [CrossRef]
14. Chang, L.L.; Wang, Y.D.; Ren, Y. In-situ investigation of stress-induced martensitic transformation in Ti–Nb binary alloys with low Young's modulus. *Mater. Sci. Eng. A* **2016**, *651*, 442–448. [CrossRef]
15. Hao, Y.L.; Li, S.J.; Sun, S.Y.; Zheng, C.Y.; Hu, Q.M.; Yang, R. Super-elastic titanium alloy with unstable plastic deformation. *Appl. Phys. Lett.* **2005**, *87*, 091906. [CrossRef]

16. Matsumoto, H.; Watanabe, S.; Hanada, S. Beta TiNbSn alloys with low Young's modulus and high strength. *Mater. Trans.* **2005**, *46*, 1070–1078. [CrossRef]
17. Hao, Y.L.; Li, S.J.; Sun, S.Y.; Zheng, C.Y.; Yang, R. Elastic deformation behaviour of Ti–24Nb–4Zr–7.9Sn for biomedical applications. *Acta Biomater.* **2007**, *3*, 277–286. [CrossRef] [PubMed]
18. Hanada, S.; Masahashi, N.; Jung, T.K. Effect of stress-induced α″ martensite on Young's modulus of β Ti-33.6Nb-4Sn alloy. *Mater. Sci. Eng. A* **2013**, *588*, 403–410. [CrossRef]
19. Jung, T.-K.; Semboshi, S.; Masahashi, N.; Hanada, S. Mechanical properties and microstructures of β Ti-25Nb-11Sn ternary alloy for biomedical applications. *Mater. Sci. Eng. C* **2013**, *33*, 1629–1635. [CrossRef] [PubMed]
20. Obbard, E.G.; Hao, Y.L.; Talling, R.J.; Li, S.J.; Zhang, Y.W.; Dye, D.; Yang, R. The effect of oxygen on α″ martensite and superelasticity in Ti–24Nb–4Zr–8Sn. *Acta Mater.* **2011**, *59*, 112–125. [CrossRef]
21. Jabir, H.; Fillon, A.; Castany, P.; Gloriant, T. Crystallographic orientation dependence of mechanical properties in the superelastic Ti-24Nb-4Zr-8Sn alloy. *Phys. Rev. Mater.* **2019**, *3*, 063608. [CrossRef]
22. Kafkas, F.; Ebel, T. Metallurgical and mechanical properties of Ti-24Nb-4Zr-8Sn alloy fabricated by metal injection molding. *J. Alloys Compd.* **2014**, *617*, 359–366. [CrossRef]
23. Hao, Y.L.; Zhang, Z.B.; Li, S.J.; Yang, R. Microstructure and mechanical behavior of a Ti–24Nb–4Zr–8Sn alloy processed by warm swaging and warm rolling. *Acta Mater.* **2012**, *60*, 2169–2177. [CrossRef]
24. Bertrand, E.; Castany, P.; Yang, Y.; Menou, E.; Couturier, L.; Gloriant, T. Origin of {112}<111> antitwinning in a Ti-24Nb-4Zr-8Sn superelastic single crystal. *J. Mater. Sci.* **2022**, *57*, 7327–7342. [CrossRef]
25. Chou, K.; Marquis, E.A. Oxygen effects on ω and α phase transformations in a metastable β Ti-Nb alloy. *Acta Mater.* **2019**, *181*, 367–376. [CrossRef]
26. Liu, J.P.; Wang, Y.D.; Hao, Y.L.; Wang, H.L.; Wang, Y.; Nie, Z.H.; Su, R.; Wang, D.; Ren, Y.; Lu, Z.P.; et al. High-energy X-ray diffuse scattering studies on deformation-induced spatially confined martensitic transformations in multifunctional Ti–24Nb–4Zr–8Sn alloy. *Acta Mater.* **2014**, *81*, 476–486. [CrossRef]
27. Li, X.; Ye, S.; Yuan, X.; Yu, P. Fabrication of biomedical Ti-24Nb-4Zr-8Sn alloy with high strength and low elastic modulus by powder metallurgy. *J. Alloys Compd.* **2019**, *772*, 968–977. [CrossRef]
28. Yang, Y.; Castany, P.; Cornen, M.; Thibon, I.; Prima, F.; Gloriant, T. Texture investigation of the superelastic Ti–24Nb–4Zr–8Sn alloy. *J. Alloys Compd.* **2014**, *591*, 85–90. [CrossRef]
29. Yang, Y.; Castany, P.; Cornen, M.; Prima, F.; Li, S.J.; Hao, Y.L.; Gloriant, T. Characterization of the martensitic transformation in the superelastic Ti–24Nb–4Zr–8Sn alloy by in situ synchrotron X-ray diffraction and dynamic mechanical analysis. *Acta Mater.* **2015**, *88*, 25–33. [CrossRef]
30. Coakley, J.; Rahman, K.M.; Vorontsov, V.A.; Ohnuma, M.; Dye, D. Effect of precipitation on mechanical properties in the β-Ti alloy Ti–24Nb–4Zr–8Sn. *Mater. Sci. Eng. A* **2016**, *655*, 399–407. [CrossRef]
31. Church, N.L.; Talbot, C.E.P.; Jones, N.G. On the influence of thermal history on the martensitic transformation in Ti–24Nb–4Zr–8Sn (wt%). *Shape Mem. Superelasticity* **2021**, *7*, 166–178. [CrossRef]
32. Hein, M.; Lopes Dias, N.F.; Pramanik, S.; Stangier, D.; Hoyer, K.-P.; Tillmann, W.; Schaper, M. Heat treatments of metastable β titanium alloy Ti–24Nb–4Zr–8Sn processed by laser powder bed fusion. *Materials* **2022**, *15*, 3774. [CrossRef] [PubMed]
33. Church, N.L.; Jones, N.G. The influence of stress on subsequent superelastic behaviour in Ti2448 (Ti–24Nb–4Zr–8Sn, wt%). *Mater. Sci. Eng. A* **2022**, *833*, 142530. [CrossRef]
34. Church, N.L.; Connor, L.D.; Jones, N.G. The effect of sample size on the microstructure and mechanical properties of Ti2448 (Ti–24Nb–4Zr–8Sn wt%). *Scr. Mater.* **2023**, *222*, 115035. [CrossRef]
35. Church, N.L.; Talbot, C.E.P.; Connor, L.D.; Michalik, S.; Jones, N.G. Functional fatigue during superelastic load cycling of Ti2448 (Ti–24Nb–4Zr–8Sn, wt%). *Materialia* **2023**, *28*, 101719. [CrossRef]
36. Church, N.L.; Talbot, C.E.P.; Miller, J.R.; Connor, L.D.; Michalik, S.; Jones, N.G. Evidence of dislocation dependent behaviour in superelastic Ti2448 (Ti–24Nb–4Zr–8Sn, wt%). *Acta Mater.* **2023**, *255*, 119066. [CrossRef]
37. Church, N.L.; Talbot, C.E.P.; Connor, L.D.; Michalik, S.; Jones, N.G. The interdependence of the thermal and mechanical cycling behaviour in Ti2448 (Ti–24Nb–4Zr–8Sn, wt%). *Mater. Sci. Eng. A* **2024**, *889*, 145791. [CrossRef]
38. Challis, V.J.; Xu, X.; Halfpenny, A.; Cramer, A.D.; Saunders, M.; Roberts, A.P.; Sercombe, T.B. Understanding the effect of microstructural texture on the anisotropic elastic properties of selective laser melted Ti–24Nb–4Zr–8Sn. *Acta Mater.* **2023**, *254*, 119021. [CrossRef]
39. Reed, O.G.; Church, N.L.; Jones, N.G. Understanding the room temperature recovery behavior in a Ti–24Nb–4Zr–8Sn superelastic alloy. *Adv. Eng. Mater.* **2024**, *26*, 2400076. [CrossRef]
40. Church, N.L.; Ang, J.Y.; Reed, O.G.; Gibson, O.E.; Jones, N.G. The effect of athermal omega on the transformation behaviour of Ti–24Nb–4Zr–8Sn (wt%). *Materialia* **2024**, *38*, 102266. [CrossRef]
41. Reed, O.G.; Desson, B.T.; Church, N.L.; Jones, N.G. The effect of the rolling reduction ratio on the superelastic properties of Ti–24Nb–4Zr–8Sn (wt%). *Metals* **2025**, *15*, 1323. [CrossRef]

42. Coakley, J.; Isheim, D.; Radecka, A.; Dye, D.; Stone, H.J.; Seidman, D.N. Microstructural evolution in a superelastic metastable beta-Ti alloy. *Scr. Mater.* **2017**, *128*, 87–90. [CrossRef]
43. Yang, C.L.; Zhang, Z.J.; Li, S.J.; Liu, Y.J.; Sercombe, T.B.; Hou, W.T.; Zhang, P.; Zhu, Y.K.; Hao, Y.L.; Zhang, Z.F.; et al. Simultaneous improvement in strength and plasticity of Ti–24Nb–4Zr–8Sn manufactured by selective laser melting. *Mater. Des.* **2018**, *157*, 52–59. [CrossRef]
44. Liang, Q.; Zheng, Y.; Wang, D.; Hao, Y.; Yang, R.; Wang, Y.; Fraser, H.L. Nano-scale structural non-uniformities in gum like Ti–24Nb–4Zr–8Sn metastable β-Ti alloy. *Scr. Mater.* **2019**, *158*, 95–99. [CrossRef]
45. Liang, Q.; Wang, D.; Zheng, Y.; Zhao, S.; Gao, Y.; Hao, Y.; Yang, R.; Banerjee, D.; Fraser, H.L.; Wang, Y. Shuffle-nanodomain regulated strain glass transition in Ti–24Nb–4Zr–8Sn alloy. *Acta Mater.* **2020**, *186*, 415–424. [CrossRef]

https://doi.org/10.3390/met16070736